Using Parameterization and Springs to Determine Aneurysm Wall Thickness

Erick Johnson, Yongjie Zhang, and Kenji Shimada

Carnegie Mellon University, 5000 Forbes Ave. Pittsburgh, PA 15289
eljohnso@andrew.cmu.edu, jessicaz@andrew.cmu.edu, shimada@cmu.edu

Abstract. Aneurysms are an enlargement of a blood vessel due to a weakened wall and can pose significant health risks. Abdominal aortic aneurysms alone are the 13th leading cause of death in the United States, with 15,000 deaths annually. While there are recommended guidelines for doctors to follow in the treatment of specific aneurysms, they cannot guarantee a satisfactory outcome. Computer simulations of an aneurysm may be able to help doctors in their treatment; however, the results are inaccurate if the vessel wall thickness is poorly measured. In order to provide more accurate, patient-specific simulations, not only does geometry for the fluid domain need to be created from medical images for analysis, but the creation of more accurate models for the wall needs to be accomplished as well. This paper proposes a solution to the latter by deforming the mesh from a healthy vessel into one with an aneurysm through parameterization and the use of a spring model. The thickness of the resulting wall model is empirically valid and fluid-structure interaction simulations show significant improvements when using a variable versus a uniform wall thickness.

Keywords: Aneurysm, Deformation, Parameterization, Spring System.

1 Introduction

Aneurysms are an enlargement of a blood vessel due to a weakened wall, and simulating them is an area of significant research and concern. They can occur anywhere in the vascular system, though are most common along the abdominal aorta and in the brain. The simulation of aneurysms is of critical importance because of the large health risk they pose. Rupturing of an abdominal aortic aneurysm (AAA) occurs in 1–3% of men aged 65 or older and is 70–95% fatal [7]. This paper presents a method to approximate the wall thickness of patient-specific geometry, which will increase the accuracy of simulations.

While there are recommended guidelines for doctors to follow in the treatment of specific aneurysms, they cannot guarantee a satisfactory outcome. Even with the guidelines for AAAs [7], a lot is left to the best judgment of the

doctor due to the many variables. Smokers between the ages of 65–75 are encouraged to have a screening, while it is elective for non-smokers. An annual checkup is recommended if the aneurysm is larger than 4 cm in diameter, otherwise it is not a primary health risk. If open surgery is deemed necessary, there is a 4–5% chance of mortality with almost 33% of patients developing other complications. The rupture of cerebral aneurysms are harder to predict and have a much more varied outcome. Some victims may suffer no complications while it is fatal to others. Being able to better predict the growth and failure of the vessel wall or, in the future, the outcome of surgical procedures, could significantly decrease the mortality rate of patients with aneurysms.

Computer simulations are starting to be used to simulate blood flow through aneurysms in order to predict and better understand ruptures. This entails creating geometry of the patient's aneurysm from medical images and running a computational fluid dynamic (CFD) or fluid-structure interaction (FSI) analysis. In addition to all of the other aspects involved in providing doctors with *instantaneous* simulations, a major setback is accurately measuring the thickness of blood vessel walls. A doctor will not rely on an analysis if the results vary by an order-of-magnitude due to poor wall thickness data. In order to provide increasingly precise, patient-specific simulations, not only does the geometry for the fluid domain need to be created, but the creation of a more accurate wall model needs to be accomplished as well.

This paper presents a method to improve the accuracy of FSI simulations for aneurysms by estimating the wall thickness with the blood vessel geometry. The proposed method maps two geometries onto the same domain in order to deform one into the other. This deformation is achieved through two steps. First, parameterization is used to move the mesh from the healthy blood vessel onto the aneurysm, which provides the initial configuration of the spring system. Second, the numerical relaxation of a spring system allows the forces between the nodes to balance in a way that approximates the stretching of the vessel wall. FSI analyses are used to test the results of the variable wall thickness and compare it against the solution for a uniform wall.

The paper continues in the next section with a discussion of previous work. Section 3 provides a description of the method to calculate the aneurysm wall thickness with Section 4 explaining the boundary-layer meshing scheme used to prepare the models for the analyses. The results found in the FSI analyses of the aneurysm models are presented in Section 5. The paper is concluded in Section 6 with a discussion and future work.

2 Previous Work

In computer simulations, the wall thickness plays a key role in determining the shear stress on the vessel wall. In order to provide a patient-specific simulation, accurate modeling of the target area is required. A lot of work is being done to create models from medical images for use in simulations, see the work of Zhang *et al.* for an example of creating smooth geometry with

NURBS (Nonuniform Rational B-Splines) [33]. While there is a push to automate this part of the process, significant user input is still required for proper classification and segmentation. In many cases the wall thickness is not measurable from the image data. Even though AAA walls can be seen in medical images, an exact thickness is hard to determine, especially in the thinnest regions. This is because the typical CT scan has a resolution of about one millimeter [15]. Higher doses of X-rays can be used to achieve sub-millimeter dimensioning, but pose a greater risk to the patient. Additionally, vessel wall-thickness cannot be seen for smaller vessels, such as those found in the brain. Intravascular ultrasound (IVUS) can be used to image coronary arteries with 0.2 mm accuracy [5]. However, this is near the limit of successfully capturing the thinnest regions in a AAA and, besides not being usable in narrower vessels, i.e. cerebral arteries, it cannot resolve a thinner wall thickness.

In order to perform CFD simulations, a mesh of the fluid domain is required. Two popular methods are the advancing front [10, 16, 22] and octree [34, 13]. An advancing front approach builds a mesh off the surface, in the region of the boundary layer, and then fills the remaining space. Garimella and Shephard give a comprehensive explanation of how to generate an all tetrahedral mesh with anisotropic elements in the boundary layer [10]. A variation of this is given by Khawaja, where the boundary-layer elements remain wedges, producing a hybrid mesh [16]. Sahni *et al.* were able to obtain more accurate wall shear stress (WSS) results by using an adaptive approach to improve an existing boundary-layer mesh. Using the solution to generate tensors at the boundary-layer nodes, the anisotropy in the mesh could be changed to improve the solution [22]. Using an octree mesh provides a significantly more structured interior mesh, but is typically thought to have poorer quality near the boundary. Zhang uses pillowing near the boundary to create higher-quality elements that are also aligned with the flow near the surface [34]. Isaksen *et al.* have used these meshes to run FSI analyses on cerebral aneurysms [13].

CFD and FSI analyses are used to study the blood flow and WSS through localized regions, e.g. aneurysms, and through significantly larger portions of the vascular system [12, 26, 6, 22, 31, 19, 25, 29, 1, 34]. Torii showed the impact of both the cerebral aneurysm shape and the use of FSI on the flow and stress results [29]. Using an assumed 0.3 mm uniform wall thickness, Torii *et al.* found a 20% decrease in WSS when using compliant, instead of rigid, walls. A similar result was found by Bazilevs through a range of cerebral aneurysm models [1]. These models again assumed a uniform wall thickness because patient values are near impossible to obtain. Scotti *et al.* showed upwards of a 400% increase in WSS when a variable wall-thickness is used over its uniform wall-thickness counterparts [26, 25]. The thickness of the wall used for their aneurysms is a predetermined range that falls within the measured data from Raghavann [21]. In Raghavan's work AAAs from four cadavers were cut into strips and measured to determine a tensile yield stress for the vessel-wall tissue. It was found that the thickness varied from about

1.5 mm in the healthy regions of the aorta (approximately 15% of the radius) to a minimum of 0.23 mm at a rupture site.

Parameterization is used frequently for model texturing and surface decimation [4, 8, 17, 27, 23, 32]. It takes three-dimensional geometry and projects it onto a planar (or series of planar) domain(s) — this is not completely true as there are some methods that projects the mesh onto the surface of a sphere. A proper map should yield a one-to-one relationship between any point on itself to its parent surface. Sheffer wrote a survey in 2006 describing much of the work on linear mapping [27]. A lot of the mapping schemes will only fit elements onto convex domains and depending on the parameterization scheme different guarantees can be made about the quality. For more complex domains, i.e. closed solids or n-manifold surfaces, it is common to partition the shape into smaller, manifold regions. Kim and Yin showed alternative methods for mapping multiply connected discs. Kim *et al.* used Ricci flow to move a face with holes, for the mouth and eyes, onto an annulus in order to perform expression recognition [17]. Slit mapping was presented by Yin to show a linear solution to the same problem with the ability to set arbitrary boundaries to the inner and outer ring [32].

Model deformation is commonly accomplished through the use of mass-spring systems [28, 11, 2, 3]. Using elasticity theory, a stiffness matrix could be created and solved to model and animate the deformation of rigid bodies [28]. This however can become computationally expensive as the domain increases in complexity. Gudukbay showed solving local spring equations was a good substitute to the older methods and could still provide time-dependent deformations [11]. Both Chen and Cui have recent work for haptic feedback with surgery simulations that utilizes mass-spring systems to provide displacement and force information to the user [2, 3]. It should be noted that the blood-vessel tissue is constantly trying to repair itself and while an aneurysm is growing the walls are slowly becoming stronger as well. Kroon and Holzapfel have an finite element simulation that incorporates the growth and breakdown of collagen in the creation of a cerebral aneurysm [18].

Most of the previous vascular modeling methods have used walls with a uniform thickness when performing analyses. Some methods are beginning to use variable thicknesses, but these tend to be coarse approximations with simple geometry. This paper will present a better approximation to the wall thickness by deforming a healthy blood vessel into one with an aneurysm.

3 Wall-Thickness Estimation

To determine the aneurysm wall thickness a combination of parameterization and spring relaxation is used. The proposed method tries to mimic the process of aneurysm growth by assuming the amount of tissue remains relatively constant while the vessel wall is stretched. If a single surface-mesh can be placed on both the healthy and aneurysm geometries then the change in area of the elements should also represent a local change in wall thickness.

As outlined in Figure 1, the mapping provides a way to move the surface triangulation from the deforming vessel, S_0, onto the surface of the aneurysm, S_1. While the two meshes now lie on the same domain, the deformed surface, S_2, is not a physically meaningful solution. A spring system is used to approximate the elastic nature of the vessel tissue and its relaxation allows the nodes of the deformed mesh to shift their locations along the aneurysm surface. This provides a solution, S_3, that better reflects how the healthy vessel was deformed. By comparing the original and deformed mesh, the wall thickness can be found through a simple volume preserving calculation.

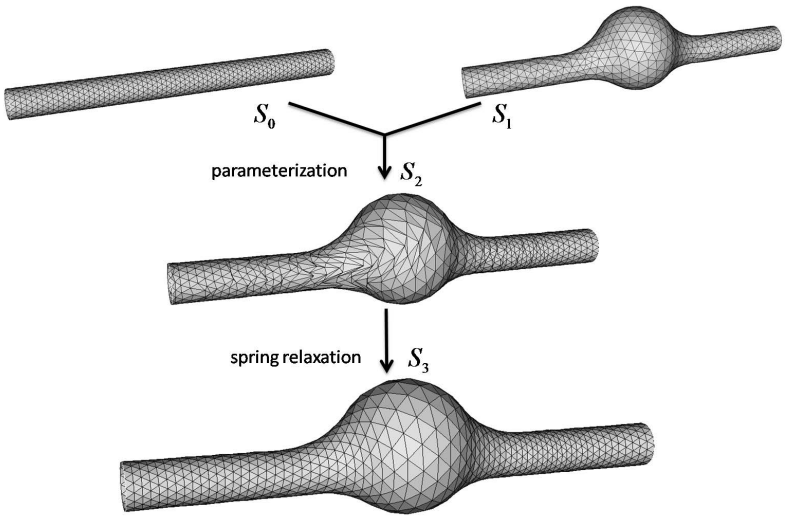

Fig. 1. Deformation of a fusiform aneurysm: S_0 and S_1 are combined in a map to create S_2. S_3 is the spring-relaxed model of S_2. S_0 and S_1 contain 2272 and 1720 triangles respectively.

3.1 Deformation through Parameterization

Moving the mesh from the healthy blood vessel onto the geometry of the aneurysm is achieved in three steps. First, the meshes for the healthy and aneurysm models are mapped onto annuli. Second, both maps are overlaid, which allows nodes from the healthy-surface map to be matched to a unique location in the map of the aneurysm. Third, using this relationship, nodes from the healthy mesh can be moved onto the desired geometry.

In order to create the mappings, the surface being *deformed*, S_0, and the *desired* surface, S_1, will need to be triangulated, t_0 and t_1 respectively. A model is required for both the desired, aneurysm shape and the deforming, healthy, blood vessel. While the aneurysm model can be created from the segmentation of medical images, unless a model already exists for the healthy vessel, an approximation will be required. An advancing front method is

used to create a uniform triangulation on S_0 and is recommended to avoid weighting issues while smoothing with the spring system. The triangle mesh creates M nodes on the surface, with m nodes, $n_i, i = 1, ..., m$, being interior to those nodes on the boundary, $n_i, i = m + 1, ..., M$. Every node, n_i, has coordinates on the surface, x_i, and a set of valent nodes, V_i.

The nodes from S_0 and S_1 are mapped onto an annulus using a uniform parameterization in polar coordinates, see Figures 2(a) and 2(c). The annulus is chosen as the working domain primarily because it matches the topology of a cylinder and is still robust for geometries with multiple branches. Each surface has an inlet and outlet that are forced, respectively, onto the outer and inner rings of the annulus. This is accomplished through homogeneous coordinate transformations that translate and rotate each curve onto the same plane and scales them to the proper radii. The radii of the inner, $r_{in} = 1$, and outer, $r_{out} = 10$, rings can be different values, and does not change the final results. All the remaining nodes are then projected normally onto the annulus' plane so the iterative solution can be calculated in two-dimensions instead of three, see Figure 2(b).

Many weighting schemes used for parameterization are meant for convex domains, and as a result, solving the system over an annulus produces triangles that are tangled and fall outside the its bounds. This can be circumvented by moving the calculations of Equation (1) into the polar space. Using a uniform parameterization [30],

$$\acute{x}_i = \sum_{j \in V_i} \frac{\acute{x}_j}{v_i}, \tag{1}$$

places each node in the geometric center of its neighbors, where v_i is the valence number of node n_i. The initial, strict projection of the nodes directly onto the plane may create tangled triangles; however, iterating over the interior nodes with Equation (1) will pull them apart, see Figure 2(c). While most of the triangles will be highly anisotropic, they will also be untangled in polar coordinates. Unfortunately a few inverted triangles may appear when moving back to a Cartesian frame. These can be made positive with a couple iterations of an algorithm presented by Freitag. It is used to maximize the area of the triangles around every node [9]. At each node, a patch is constructed with its neighboring triangles and the minimum area is maximized. This yields a valid triangulation with the same topology in $\Re^2$ as the surfaces in $\Re^3$. The maps only need untangled triangles in order to provide the one-to-one relationship. Higher-quality elements in the maps may improve the initial deformation, but are not critical to the overall method.

The projected nodes now have coordinates $\acute{x}_i$ on the annulus and the projected triangles are $\acute{t}_i$. As can be seen in Figure 2, a uniformly meshed cylinder will appear very regular, with the triangles becoming increasingly skewed as their radial location increases. This is in contrast to the map of S_1, showing a denser concentration of triangles on the side corresponding to the offset aneurysm.

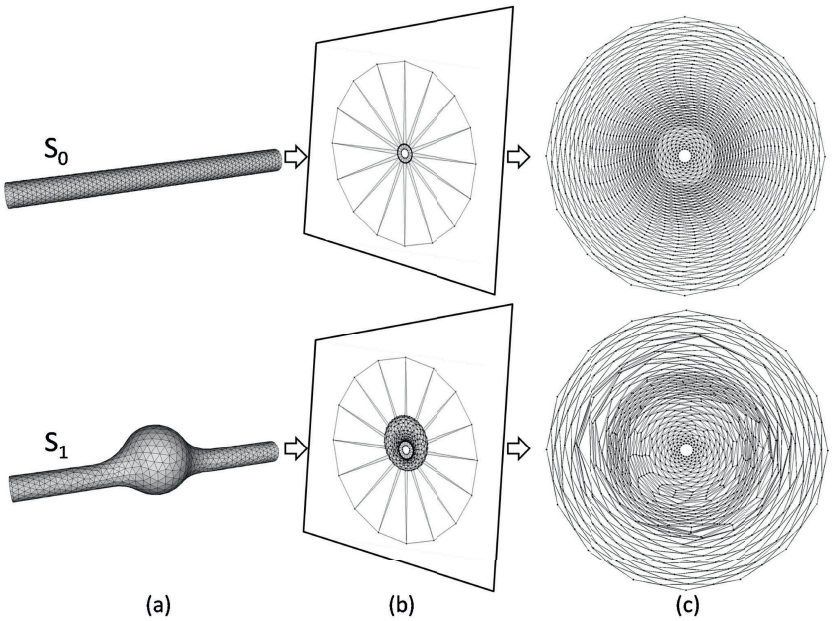

Fig. 2. Mapping of the nodes from a surface to the annulus; (b) shows the initial projection of nodes onto the annuli's plane. (c) shows the final maps after iterating with Equation (1).

The overlay of the two maps provides the relationship needed between the nodes from S_0 and the triangles from S_1, see Figure 3(c). With both maps overlaid, each non-boundary node, $n_{0,i}$, can be found to lie in a triangle, $\acute{t}_{1,j}$, as shown in Figure 3(c) pullout. As a result of the maps covering the same domain and having no tangled elements, *every* node in the map of S_0 will correspond to a unique point within the map of S_1. Further, by knowing every point within $\acute{t}_{1,j}$ also lies uniquely in its surface counterpart, $t_{1,j}$, locating the barycentric coordinates of $\acute{x}_{0,i}$ in $\acute{t}_{1,j}$ also defines its location, $x_{2,i}$, in $t_{1,j}$ on S_1, see Figure 3(d). Finding which triangle each node lies in starts with a search for the coordinate in the map of S_1 that yields the shortest distance to $\acute{x}_{0,i}$. Any triangle connected to that location is chosen as the initial guess for $\acute{t}_{1,j}$, with the surrounding triangles being moved through until all the barycentric coordinates are positive for $\acute{x}_{0,i}$.

Once the barycoordinates of all the nodes, $n_{0,i}$, have been found, they create the resultant surface, S_2. The healthy, blood vessel now matches the *shape* of the vessel with the aneurysm. Unfortunately, this alone does not provide accurate enough information to calculate the wall thickness. As a result of the weighting scheme used in the map, the parametric transformation between two different surfaces is not guaranteed to be the same, *i.e.* if the inner and outer radii of the annulus are 1 and 10 respectively, r = 5 may

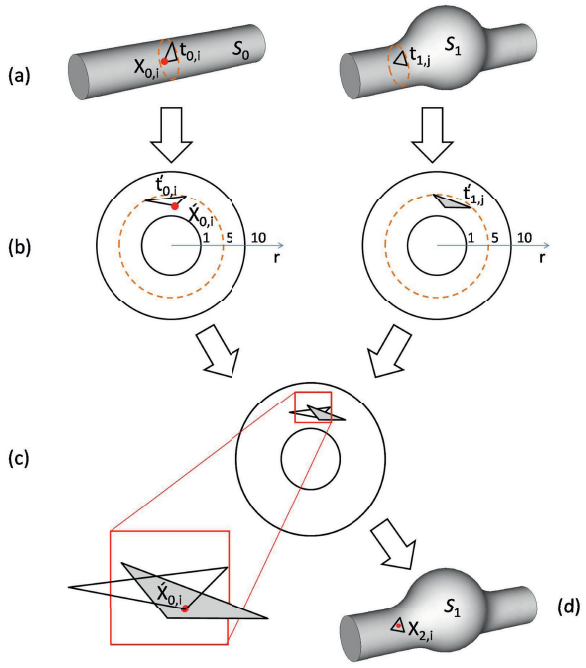

Fig. 3. Overview of the deformation following a node from S_0 (the red dot). (a) The original surface. (b) The map of a surface on its annulus resulting in the mapping of t_i into $\acute{t}_i$. The dashed line represents the location of r = 5 on both surfaces and the map. (c) An overlay of the maps allows the barycentric coordinates for $\acute{x}_{0,i}$ within $\acute{t}_{1,j}$ to be found. (d) The barycoordinates found in (c) are the same for $x_{2,i}$ in $t_{1,j}$ and move the nodes from S_0 onto S_1.

not correspond to the same axial coordinate in the original geometry, see Figures 3(a) and 3(b). Consequently, using the mapping technique, *by itself*, will create a bias as to where the wall is thinnest and not represent the true deformation. By converting the mesh into a spring system and allowing the nodes to move, this can easily be corrected.

3.2 Relaxation Using Springs

To make the deformation physically meaningful the deforming geometry should not only match the shape of the desired model, but the elements should stretch in an elastic manner. That is, a blood vessel will have deformed more significantly near the aneurysm than its ends, and the triangulation of S_2 should represent that properly. In order to accomplish this, a linear spring system is created from the mesh, *i.e.* the edges of the triangles become springs attached at the nodes. Through a series of iterations the springs are relaxed until their displacement is below some threshold; here it is less than 5% of

the shortest edge. Additionally, the nodes are projected back onto S_1, in a direction normal to the surface, after every iteration to ensure S_2 does not deviate from the desired shape. Equation (2) calculates the force, F_i, acting on every node by comparing the current length of each attached spring against its undeformed length,

$$F_i = k \sum_{j \in V_i} l_{i,j} - ||x_{0,j} - x_{0,i}|| \hat{l_{i,j}}, \tag{2}$$

where $l_{i,j} = (x_{2,j} - x_{2,i})$ is the vector of the current spring between nodes $n_{2,j}$ and $n_{2,i}$ and $\hat{l_{i,j}}$ is the regularized direction. For this work the spring stiffness, $k = 1$, is a constant because of the uniform mesh and the isotropic material properties assumed. Every node is then updated by,

$$x_{2,i} = x_{2,i} + s\frac{F_i}{k}, \tag{3}$$

a fraction of the distance determined by the force acting on it. The step size of $s = 0.1$ prevents the nodes from taking too large a jump and tangling. The process is outlined in Algorithm 1 and the final surface is S_3.

```
while movement > ϵ do
    for every node n_{2,i} do
        calculate force at n_{2,i} using Equation (2)
        move n_{2,i} using Equation (3)
        project n_{2,i} to S_1
    end
end
```

Algorithm 1. Spring Correction

The deformed, blood vessel now matches the shape of the aneurysm and takes the elasticity of the vessel tissue into account. Even though this spring model can only provide a linear approximation, it is a first guess at trying to represent the complex elasticity and anisotropic nature of the tissue. However, steps can be taken to improve this. If t_0 is not a uniformly generated, triangle mesh, then each spring will need a stiffness relative to its original length in S_0. Additionally, since the axial and circumferential stiffness of the tissue are different, the material properties of tissue should be incorporated through a change in the spring constant as well. A non-linear spring system may also prove to represent the true elastic nature of the tissue more completely.

3.3 Thickness Calculation

The wall thickness at every node in S_3 can now be calculated. The deformed mesh has elements of different sizes than originally and because the topology

was never altered, the change in area between $t_{0,i}$ and $t_{3,i}$ can be compared directly. Since the Poisson's ratio of tissue is near 0.5, the change in wall thickness will be inversely proportional to the change in an elements area. At each node $n_{3,i}$, the wall thickness, $d_{3,i}$, is related to the average ratio of the change in area of the neighboring triangles,

$$d_{3,i} = d_{0,i} \frac{\sum_{j \in V_i} \frac{A_{0,j}}{A_{3,j}}}{v_i}, \tag{4}$$

where $A_{0,j}$ and $A_{3,j}$ are the area of triangles $t_{0,j}$ and $t_{3,j}$ respectively and $d_{0,i}$ is the initial thickness, which is assumed to be uniform.

Geometry and a mesh for the blood vessel wall could be created directly from this information. It should be noted that while S_3 has the wall thickness values associated with the location of its nodes, S_1 has a significantly higher quality mesh because it was never stretched. The barycentric coordinates of $n_{1,i}$ within $t_{3,j}$ should be used to map the wall thicknesses to S_1 since the geometry of S_1 and S_3 match. Figure 4 shows the final wall thickness, the outermost layer, and the fluid mesh, which is discussed in Section 4. As can be seen in the figure, there can be a significant change in the wall thickness through a very small distance.

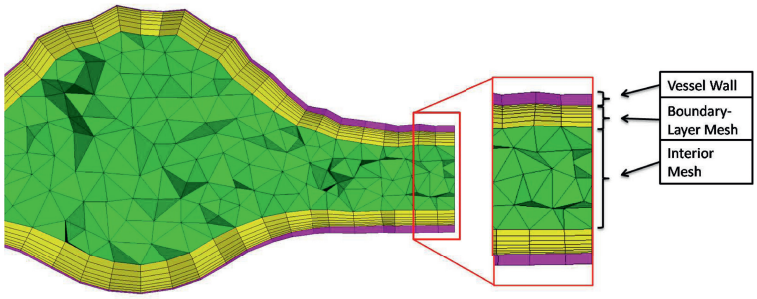

Fig. 4. The vessel wall (3440 wedges) with the boundary-layer mesh (17200 wedges) and interior mesh (6913 tetrahedra) for a fusiform aneurysm.

4 Boundary-Layer Meshing

Once the wall thickness has been found, a mesh of the fluid domain needs to be generated in order to run FSI simulations. To properly capture the rapidly changing velocity within the boundary layer, anisotropic wedges are used along the walls and created in an advancing-front manner [14]. Every surface node has a direction and size that controls the growth of the wedges to prevent a collision of fronts and tangling of elements. After a specified number of layers have been generated, the remaining space is filled with tetrahedra.

The growth of the boundary-layer mesh is dictated by a hair at each node. A hair is a vector connected to a node. The initial direction of the hair is

the normal of the surface, while its length is chose to provide near isotropic elements in the outermost layer. The hairs are then smoothed to make sure the wedges do not tangle.

Smoothing the direction is accomplished by moving a hair to the average of its neighbors. If the difference between the hair and the average is larger than 30° the hair is instead moved iteratively to allow its neighbors to move towards it as well. Though not common in biological models, there is a chance a hair could point outside the volume. In these rare instances the hair is marched towards a location where the dot product between it and all the neighboring surfaces is positive, if it exists.

The length of the hair is then smoothed with regards to both the geometry and its neighbors. Concerning the geometry, using a uniform length for every hair would produce increasingly skewed elements near sharp corners. To remedy this, the length of a hair is increased relative to the angle of the corner. This ensures perpendicular corners remain perpendicular. Additionally, a hair's length should also be smoothed with respect to its neighbors. Using the average length would cause a ballooning of the boundary-layer mesh around corners. Instead, the length becomes the average of the normal component of its neighbors' hairs.

Even though the boundary-layer mesh can now grow with well-shaped elements, there is still a chance for fronts from competing surfaces, and even adjacent hairs in high-curvature regions, to intersect. To avoid these collisions, a sizing function based on the radius of the medial-ball is used [20]. The radius of the medial-ball is placed in a background octree-mesh and the values are smoothed with a quadratic, inverse-distance weighted interpolation. If the length of a hair is larger than the local sizing-function, it is shortened. This method for collision avoidance allows a wider range of length scales to be present in the biological models without having to specify proper sizing for each part of the boundary-layer mesh.

5 Results

Models for the fluid region of a fusiform and saccular aneurysm were created to represent both the healthy blood vessel and one with an aneurysm. A fusiform aneurysm occurs when the entire circumference of the blood vessel dilates, though it is commonly not axisymmetric. A saccular aneurysm is where the growth occurs in a small region of the wall and exhibits necking. With these models, the method presented was used to deform the healthy vessel into the unhealthy one in order to yield geometry with a varying thickness for the wall. These were compared against measured values for wall thickness and FSI analyses were performed to validate the method against expected results.

As shown in Figure 1, the healthy geometry for the fusiform set was a cylinder with a diameter of 2 cm and a length of 24 cm. The aneurysm, with a diameter of 6 cm, was placed in the center of the healthy vessel with an

offset from the axis of 0.75 cm. The initial wall thickness was calculated to be 1.50 mm. After deformation, the minimum wall thickness was found to be 0.22 mm, with an average of 1.11 mm. The deformation can be seen in Figure 1 and the final wall in Figure 4. With 2272 triangles and 1152 nodes in S_0 and 1720 triangles and 876 nodes in S_1, it took 200 s to create the parameterizations, deform the surface, relax the springs, and calculate the final wall thickness. Surgery would be recommended for an aneurysm of this size and the wall thickness is near the limit measured by [21]. The saccular aneurysm had a maximum diameter of about 4 cm and was placed off-center from the axis of the 2 cm diameter vessel. The minimum thickness of the wall was 0.41 mm with an average of 1.23 mm, see Figures 5 and 6. With 6588 triangles and 3320 nodes in S_0 and 7968 triangles and 4010 nodes in S_1 it took 2771 s to determine the wall thickness. In both cases the majority of the time was taken to relax the spring system and needs to be looked at for efficiency. All the surface were meshed using the advancing front algorithm in CUBIT [24].

The vessel wall and fluid volume of the fusiform geometry were then meshed in order to perform FSI simulations. The wall was meshed with 2 layers for a total of 3440 wedges. The wedges in the wall had a maximum dihedral-angle (MDA) range between 90°–106°. Due to the dimensions of the blood vessel, the boundary layer plays a particularly important role in the development of the flow and the resultant WSS. As a result the mesh in

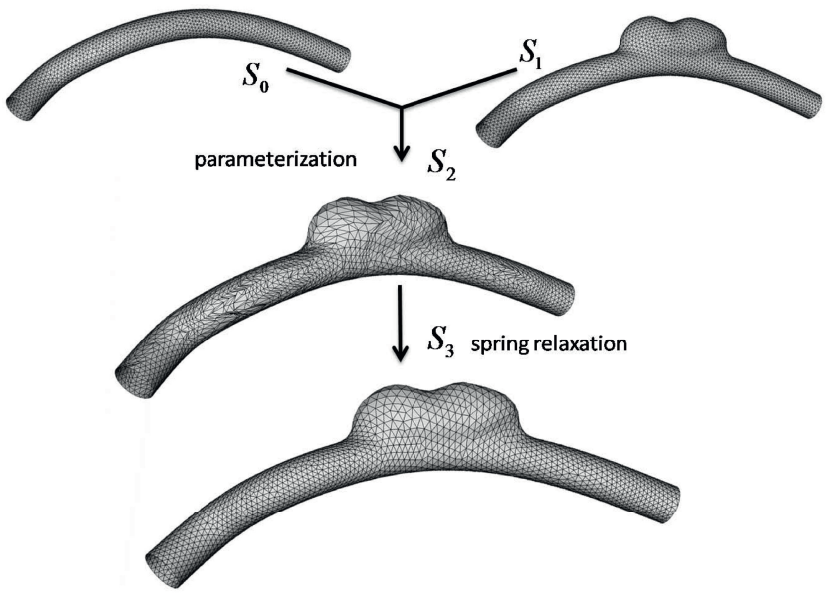

Fig. 5. Deformation process of the saccular aneurysm. S_0 and S_1 contain 6588 and 7968 triangles respectively.

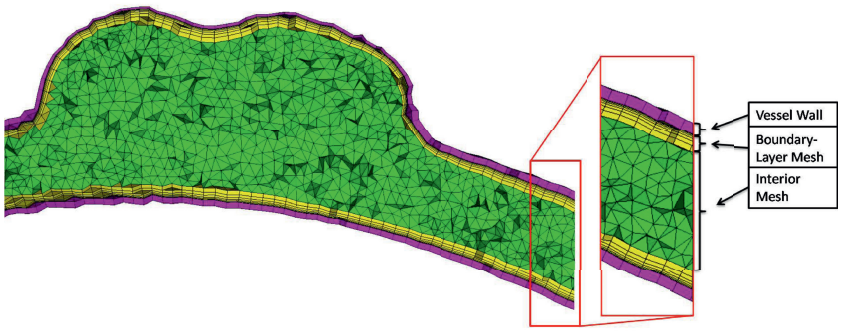

Fig. 6. The vessel wall (15936 wedges) with the boundary-layer mesh (79680 wedges) and interior mesh (57852 tetrahedra) for the saccular aneurysm.

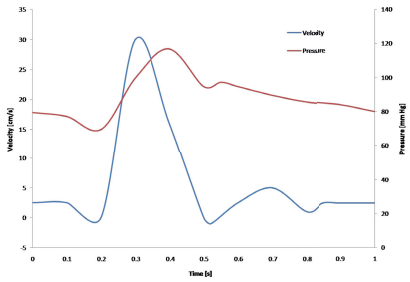

Fig. 7. The cardiac cycle used in the FSI analyses for the inlet, velocity, and outlet, pressure, boundary conditions.

the region of the boundary layer should be sized appropriately in order to capture the steep and changing gradient. The fluid-volume mesh was created using the advancing-front method presented and implemented in CUBIT for boundary-layer meshing and consisted of 17200 wedges (10 layers along the wall) and 6913 tetrahedra. There were 20 wedges with a MDA over 150° and an aspect ratio range of 2-63; the aspect ratio is the ratio between the longest and shortest edge lengths of an element. The fluid-domain tetrahedra had a MDA between 73°–135°.

The FSI analyses were run to compare the WSS and mesh displacement between simulations with uniform and variable wall thicknesses for the fusiform model. They were run with ANSYS® and ANSYS®, CFX™. The blood flow was approximated as a Newtonian fluid with a dynamic viscosity of $\mu = 3.85$ cP and solved using a shear stress transport model. A simplified representation of the cardiac cycle, Figure 7, was used to provide boundary conditions giving an inlet velocity with a peak of 31 cm/s at 0.3 s and an outlet pressure with a peak of 118 mm Hg at 0.4 s. The vessel wall was treated as an

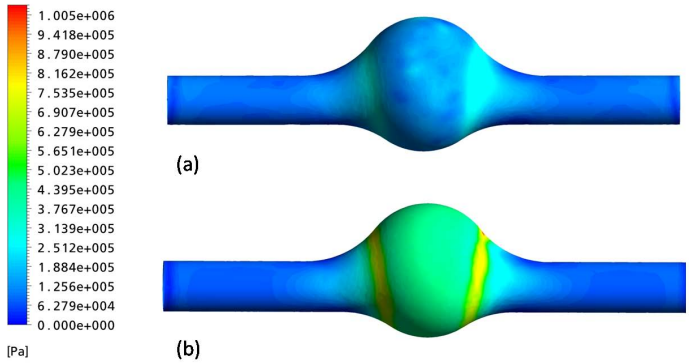

Fig. 8. The shear stress at 0.4 s for the (a) uniform and (b) variable wall thickness.

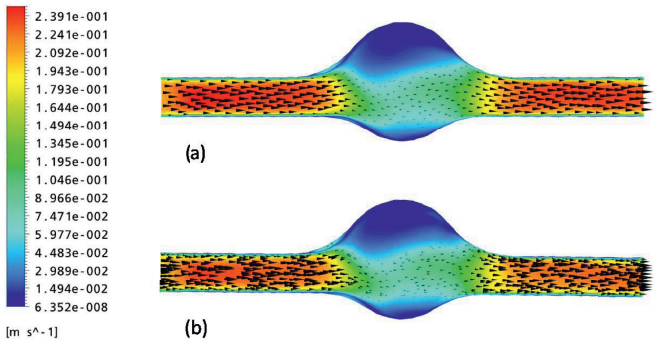

Fig. 9. The velocity with a vector field at 0.4 s for the (a) uniform and (b) variable wall thickness.

isotropic material with a Young's modulus of $E = 2.7$ MPa, a density of $\rho = 2000$ kg/m^3, and a Poisson's ratio of $\nu = 0.45$ and the ends were fixed in place.

The analysis was first performed on the geometry with a uniform wall thickness (1.5 mm). With a pulsatile flow the maximum WSS was 0.31 MPa and occurred on the anterior and posterior regions of the aneurysm, Figure 8(a). A second simulation was run using the variable wall-thickness determined by the proposed method. The results match well with what is expected. The max WSS for the variable wall thickness was 1.04 MPa at about 0.4 s and can be seen in Figure 8(b). Using a variable wall thickness produced a 330% increase in the WSS even though the aneurysm geometry was unchanged. This is similar to what was seen in the work of Scotti and is below the yield stress shown by Raghavan (a mean of 1.27 MPa). The velocity profiles, Figure 9, are fairly similar between the two runs. Small differences

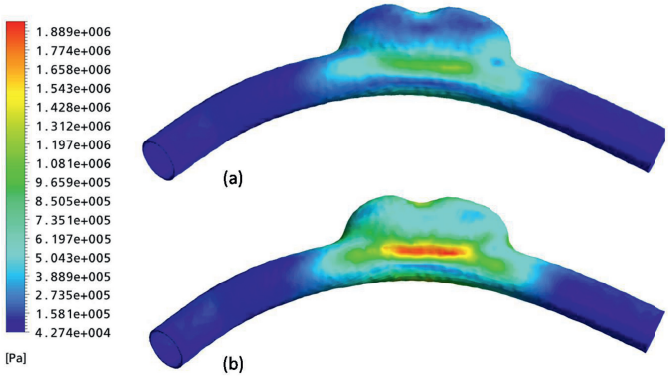

Fig. 10. The wall shear stress at 0.4 s for the saccular geometry with a (a) uniform and (b) variable wall thickness.

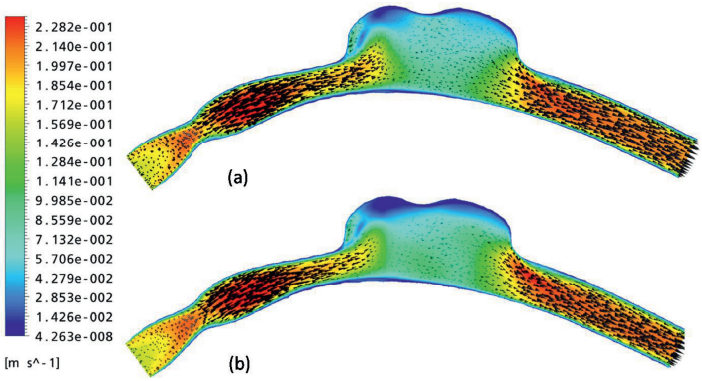

Fig. 11. The velocity with a vector field at 0.4 s for the saccular geometry with a (a) uniform and (b) variable wall thickness.

can be seen between the two though as a result of the variable wall being capable of more deformation in the thinner regions.

The same analyses was also performed on the saccular aneurysm in order to show results for a more complex model. There were 15936 wedges in the wall and 79680 in the blood volume, which also contained 57852 tetrahedra. The MDA for the tetrahedra ranged between 72°–140° in the fluid region. The wedges in the wall had a MDA between 90°–114° and in the fluid domain was between 90°–140° with an aspect ratio of 2.5–110. The analysis again showed a velocity profile that was very similar between the uniform and variable walls, a cross-section can be seen in Figure 11. The WSS, in the variable wall thickness model, had a max value of 1.89 MPa around 0.4 s and was not where failure would be predicted, see Figure 10(b). This is likely a result of the geometry created – it was not medical data – producing a stress concentration and not indicative of the method. The thinnest regions in the

variable model show a maximum WSS of 1.31 Mpa and is significantly closer to the expected value and location. There is more than a 250% increase when compared against the WSS in the same region of the uniform model (0.49 Mpa).

6 Conclusion

The proposed method provides a very good start to improve patient-specific geometry for simulations of aneurysms. Having shown how significantly the wall shear stress changes with the addition of variable wall thicknesses, it can only be argued that better predicting a patient's unique geometry is crucial. That being said, the growth of an aneurysm is more complicated than deforming an isotropic material with a uniform wall thickness. To start, the blood-vessel wall is not isotropic and repairs itself while being stretched. Moreover, as the patient ages, calcification and plaquing will locally alter the material properties and wall thickness in a way that fully predicting how the wall deforms becomes increasingly difficult. More boundary conditions should be used to simulate the natural, axial tension in the blood vessel and external pressure from surrounding organs. Regardless, having a method that can start to provide patient-specific wall geometry is a needed step.

Future work will start to incorporate some of these ideas through the use of non-linear, anisotropic springs. In addition to using medical image data for aneurysm geometry, more robust mappers should be used to accommodate increasingly complex geometry. Even though the examples presented were approximations of AAAs, the proposed method is extendable to any aneurysm.

References

1. Bazilevs, Y., Hsu, M.C., Zhang, Y., Wang, W., Liang, X., Kvamsdal, T., Brekken, R., Isaksen, J.: Computational vascular fluid-structure interaction: Methodology and application to cerebral aneurysms. Submitted to Biomechanics and Modeling in Mechanobiology (2009)
2. Chen, P., Barner, K.E., Steiner, K.V.: A displacement driven real-time deformable model for haptic surgery simulation. In: HAPTICS 2006: Proceedings of the Symposium on Haptic Interfaces for Virtual Environment and Teleoperator Systems, Washington, DC, USA, pp. 499–505 (2006)
3. Cui, T., Song, A., Wu, J.: Simulation of a mass-spring model for global deformation. Frontiers of Electrical and Electronic Engineering in China 4(1), 78–82 (2009)
4. Eck, M., DeRose, T., Duchamp, T., Hoppe, H., Lounsbery, M., Stuetzle, W.: Multiresolution analysis of arbitrary meshes. In: SIGGRAPH 1995: Proceedings of the 22nd annual conference on Computer graphics and interactive techniques, pp. 173–182. ACM Press, New York (1995)
5. Elliott, M.R., Thrush, A.J.: Measurement of resolution in intravascular ultrasound images. Physiological Measurement 17(4), 259–265 (1996)

6. Figueroa, C.A., Vignon-Clementel, I.E., Jansen, K.E., Hughes, T.J.R., Taylor, C.A.: A coupled momentum method for modeling blood flow in three-dimensional deformable arteries. Computer Methods in Applied Mechanics and Engineering 195(41–43), 5685–5706 (2006)
7. Fleming, C., Whitlock, E.P., Beil, T.L., Lederle, F.A.: Screening for abdominal aortic aneurysm: A best-evidence systematic review for the u.s. preventive services task force. Annals of Internal Medicine 142(3), 203–211 (2005)
8. Floater, M.S.: Parametrization and smooth approximation of surface triangulations. Computer Aided Geometric Design 14(3), 231–250 (1997)
9. Freitag, L.A., Plassmann, P.: Local optimization-based simplicial mesh untangling and improvement. International Journal for Numerical Methods in Engineering 49, 109–125 (2000)
10. Garimella, R.V., Shephard, M.S.: Boundary layer mesh generation for viscous flow simulations. International Journal for Numerical Methods in Engineering 49, 193–218 (2000)
11. Güdükbay, U., Özgüç, B., Tokad, Y.: A spring force formulation for elastically deformable models. Computers & Graphics 21(3), 335–346 (1997)
12. Hose, D.R., Lawford, P.V., Narracott, A.J., Penrose, J.M.T., Jones, I.P.: Fluid-solid interaction: Benchmarking of an external coupling of ANSYS with CFX for cardiovascular applications. Journal of Medical Engineering & Technology 27(1), 23–31 (2003)
13. Isaksen, J., Bazilevs, Y., Kvamsdal, T., Zhang, Y., Kaspersen, J.H., Waterloo, K., Romner, B., Ingebrigsten, T.: Determination of wall tension in cerebral artery aneurysms by numerical simulation. Stroke 39, 3172–3178 (2008)
14. Johnson, E., Yamakawa, S., Shimada, K., Brewer, M.L., Owen, S.J.: Generating hexahedral boundary-layer meshes for CFD simulations (Manuscript in preparation) (2009)
15. Ketcham, R.A., Carlson, W.D.: Acquisition, optimization and interpretation of x-ray computed tomographic imagery: Applications to the geosciences. Computers and Geosciences 27(4), 381–400 (2001)
16. Khawaja, A., Kallinderis, Y.: Hybrid grid generation for turbomachinery and aerospace applications. International Journal for Numerical Methods in Engineering 49, 145–166 (2000)
17. Kim, J., Wang, S., Zeng, Y., Wang, Y., Gu, X., Qin, H., Samaras, D.: Ricci flow for 3D shape analysis. In: Proceedings of IEEE International Conference on Computer Vision 2007, Rio de Janeiro, Brazil (October 2007)
18. Kroon, M., Holzapfel, G.A.: Modeling of saccular aneurysm growth in a human middle cerebral artery. Journal of Biomechanical Engineering 130(5), 051012.1–051012.10 (2008)
19. Mabotuwana, T.D.S., Cheng, L.K., Pullan, A.J.: A model of blood flow in the mesenteric arterial system. BioMedical Engineering OnLine 6, 17 (2007)
20. Quadros, W.R., Owen, S.J., Brewer, M.L., Shimada, K.: Finite element mesh sizing for surfaces using skeleton. In: Proceedings, 13th International Meshing Roundtable, Williamsburg, VA, USA, pp. 389–400 (2004)
21. Raghavan, M.L., Kratzberg, J., de Tolosa, E.M.C., Hanaoka, M.M., Walker, P., da Silva, E.S.: Regional distribution of wall thickness and failure properties of human abdominal aortic aneurysm. Journal of Biomechanics 39(12), 3010–3016 (2006)

22. Sahni, O., Müller, J., Jansen, K.E., Shephard, M.S., Taylor, C.A.: Efficient anisotropic adaptive discretization of the cardiovascular system. Computer Methods in Applied Mechanics and Engineering 195(41–43), 5634–5655 (2006)
23. Sander, P.V.: Sampling-efficient mesh parametrization. PhD thesis, Harvard University (2003)
24. Sandia National Laboratory. Cubit: Geometry and mesh generation toolkit
25. Scotti, C.M., Jimenez, J., Muluk, S.C., Finol, E.A.: Wall stress and flow dynamics in abdominal aortic aneurysms: Finite element analysis vs. fluid-structure interaction. Computer Methods in Biomechanics and Biomedical Engineering 11(3), 301–322 (2008)
26. Scotti, C.M., Shkolnik, A.D., Muluk, S.C., Finol, E.A.: Fluid-structure interaction in abdominal aortic aneurysms: Effects of asymmetry and wall thickness. BioMedical Engineering OnLine 4, 64 (2005)
27. Sheffer, A., Praun, E., Rose, K.: Mesh parameterization methods and their applications. Foundations and Trends in Computer Graphics and Vision 2(2), 105–171 (2006)
28. Terzopoulos, D., Platt, J., Barr, A., Fleischer, K.: Elastically deformable models. Computer Graphics 21(4), 205–214 (1987)
29. Torii, R., Oshima, M., Kobayashi, T., Takagi, K., Tezduyar, T.E.: Fluid-structure interaction modeling of blood flow and cerebral aneurysm: Significance of artery and aneurysm shapes. Computer Methods in Applied Mechanics and Engineering (2008) doi:10.1016/j.cma.2008.08.020
30. Tutte, W.T.: How to draw a graph. London Mathematical Society 13, 743–768 (1963)
31. Valencia, A.A., Guzmán, A.M., Finol, E.A., Amon, C.H.: Blood flow dynamics in saccular aneurysm models of the basilar artery. Journal of Biomechanical Engineering 128, 516–526 (2006)
32. Yin, X., Dai, J., Yau, S.-T., Gu, X.: Slit map: Conformal parameterization for multiply connected surfaces. In: Chen, F., Jüttler, B. (eds.) GMP 2008. LNCS, vol. 4975, pp. 410–422. Springer, Heidelberg (2008)
33. Zhang, Y., Bazilevs, Y., Goswami, S., Bajaj, C., Hughes, T.J.R.: Patient-specific vascular NURBS modeling for isogeometric analysis of blood flow. Computer Methods in Applied Mechanics and Engineering 196(29–30), 2943–2959 (2007)
34. Zhang, Y., Wang, W., Liang, X., Bazilevs, Y., Hsu, M.C., Kvamsdal, T., Brekken, R., Isaksen, J.: High fidelity tetrahedral mesh generation from medical imaging data for fluid-structure interaction analysis of cerebral aneurysms. Computer Modeling in Engineering & Science 42(2), 131–150 (2009)